



PERGAMON

Computers & Fluids 32 (2003) 891–916

computers
&
fluids

www.elsevier.com/locate/compfluid

On the extension of the AUSM+ scheme to compressible two-fluid models

H. Paillère ^{a,*}, C. Corre ^b, J.R. García Cascales ^c

^a CEA Saclay, DEN/DM2S/SFME, 91191, Gif-sur-Yvette, Cedex, France

^b ENSAM SINUMEF, 151 Boulevard de l'Hôpital, 75013 Paris, France

^c Dpto. de Ingeniería Térmica y de Fluidos, E.T.S.I. Industriales, 30202 Cartagena, Murcia, Spain

Received 18 December 2000; accepted 6 March 2002

Abstract

This paper describes the extension of the AUSM+ scheme to the four-equation isentropic and six-equation compressible two-fluid models for gas/liquid flow, using as equations of state the perfect gas law for the gas and either Tait's law or the stiffened gas law for the liquid. Numerical results on well-known two-fluid air/water flow benchmark problems, from nearly incompressible flows to fully compressible flows, are presented and discussed.

© 2002 Elsevier Science Ltd. All rights reserved.

1. Introduction

Over the last few years, the AUSM+ (advection upwind splitting method) scheme of Liou [1] has gained popularity among single phase compressible CFD practitioners, and has also found its way in many industrial codes, especially in the aeronautical sector [2–5]. The main reasons for the growing interest in this upwind differencing scheme are its simplicity and hence its low computational cost, its easy generalisation to arbitrary equations of state (EOS) [6], and its accuracy. Indeed, the AUSM+ scheme and related mass flux schemes such as AUSM-DV [7], are known to be as accurate as flux difference splitting methods such as Roe's or Osher's approximate Riemann solvers [8,9] without the cost of field-by-field wave decompositions. Of particular

* Corresponding author. Fax: +33-1-69-08-96-96.
E-mail address: henri.paillere@cea.fr (H. Paillère).

importance is the ability of the scheme to capture contact discontinuities exactly, thereby making the scheme very attractive for viscous flow computations.

Extension of the AUSM+ scheme to multi-phase flow was first performed by Liou and Edwards [10], based on the homogeneous equilibrium model (HEM), which is formally identical to the Euler equations of gas dynamics, with arbitrary EOS. This model assumes in particular that the two phases are in kinematic and thermodynamic equilibrium. Comparisons between the AUSM+ and approximate Riemann solvers such as the Roe scheme [11,12] and the characteristic flux scheme [13,14] were presented in [15], using representative EOS for water/steam flow. On-going work of interest in the area of multi-phase flow modelling using the HEM and Riemann-type solvers is that of Shyue, who computes air/water flow using a hybrid EOS based on a combination of perfect gas law to model the gas and either van der Waals [16] or stiffened gas [17] laws to model the liquid.

This paper proposes further extension of the AUSM+ scheme to more general two-phase flow models, and in particular to two-fluid models consisting of mass, momentum and energy conservation equations as well as an EOS for each phase [18]. It must be emphasized that one of the main difficulties of two-phase flow modelling is that there is no single model or set of governing equations. Mathematical models for two-phase flow are highly phenomenological in nature, and range from homogeneous models to multi-field models. Two-fluid models, obtained by averaging local field equations, enable both mechanical and thermal non-equilibrium to be taken into account, and in that respect, represent a more general model for two-phase flow.

As far as numerical methods are concerned, most Eulerian–Eulerian schemes used today in the field of multi-phase flow belong to the class of pressure-based methods, such as the ICE method of Harlow and Amsden [19]. The current generation of two-phase flow codes used in the nuclear industry are based on these robust methods, which can deal with a very wide range of flow regimes and conditions. However, because of their limited accuracy, as well as inability to model strong compressibility effects, other schemes have been investigated over the last decade, and in particular, density-based solvers which in the single phase case, have been shown to perform well at all flow speeds.

Extensions of characteristic-based upwind differencing methods to two-fluid models, described in [20–27] have thus been applied to various types of multi-phase flow, in industrial sectors ranging from nuclear thermal-hydraulics to oil transport and solid combustion. These extensions are by no means straightforward, as many difficulties need to be overcome, stemming from the non-hyperbolic nature of the governing equations, the presence of non-conservative terms, stiff source terms, complex EOS, etc. Unlike the approximate Riemann solvers and characteristic flux schemes cited above, the flux splitting at the basis of the AUSM+ scheme does not require any characteristic analysis or field by field decomposition. This is obviously an appealing aspect of the scheme, especially when dealing with non-hyperbolic models or with models whose mathematical properties depend so closely on closure laws as in two-phase flow. This property of the scheme, as well as its anticipated accuracy, motivated the present work.

In the following section, two single-pressure two-fluid models are described, together with the thermodynamic models we have chosen to represent flow of liquid water and air. Then, the discretization of these models using an AUSM+-type scheme is described, and finally, the method is evaluated on a series of well-known two-fluid test cases.

2. Two-fluid models

In this work, we shall focus on single pressure two-fluid models, written in the general form,

$$\frac{\partial \mathbf{U}}{\partial t} + \frac{\partial \mathbf{F}}{\partial x} = \mathbf{C}^{\text{nv}} + \mathbf{C}^v + \mathbf{S} \quad (1)$$

where \mathbf{U} is the vector of conserved variables, \mathbf{F} is the corresponding flux vector, \mathbf{C}^{nv} is the interfacial source term containing all the non-viscous differential terms (virtual mass term, interface pressure correction, etc), \mathbf{C}^v is the source term containing all the viscous differential terms (diffusion), and \mathbf{S} is the source term containing all the non-differential terms (gravity, phase change and interfacial drag). In this work, we shall neglect viscous terms ($\mathbf{C}^v \equiv 0$) and assume that no phase change occurs between the liquid and gas phases.

2.1. On hyperbolicity

As was mentioned in the Introduction, and as opposed to hyperbolic systems of conservation laws in gas dynamics, two-fluid models are characterised by a certain number of mathematical difficulties. First, Eq. (1) are not in conservative form because of the presence of the term \mathbf{C}^{nv} . Furthermore, the characteristic analysis of the reduced system,

$$\frac{\partial \mathbf{U}}{\partial t} + \frac{\partial \mathbf{F}}{\partial x} = \mathbf{C}^{\text{nv}} \quad (2)$$

shows that in general, two-fluid models are not hyperbolic, i.e. they admit complex characteristic values [18]. This implies in particular that in the limit of vanishing viscosity (physical or numerical), ill-posedness will manifest itself in the form of numerical oscillations. The addition of regularising terms, discussed for example in [28], can make the two-fluid models conditionally or unconditionally hyperbolic, and lead to well-posed initial value problems. Furthermore, characteristic-based schemes can be devised in which the artificial viscosity of the scheme scales with the (real) eigenvalues of the system [27]. As mentioned in the Introduction, the AUSM+ scheme does not rely on eigendecompositions, and thus does not require that system (2) be hyperbolic. Indeed, most of the computations discussed in Section 4 were performed with non-hyperbolic models. It is only when very fine meshes are used, or high frequency damping is required that we preferred the use of hyperbolic models.

2.2. Isentropic two-fluid model

The so-called “isentropic four-equation model” consists of a mass and a momentum balance equations for each phase. It can be cast in the form (1), with the following definitions:

$$\begin{aligned} \mathbf{U} &= \begin{pmatrix} \alpha_g \rho_g \\ \alpha_l \rho_l \\ \alpha_g \rho_g u_g \\ \alpha_l \rho_l u_l \end{pmatrix} & \mathbf{F} &= \begin{pmatrix} \alpha_g \rho_g u_g \\ \alpha_l \rho_l u_l \\ \alpha_g \rho_g u_g^2 + \alpha_g p \\ \alpha_l \rho_l u_l^2 + \alpha_l p \end{pmatrix} \\ \mathbf{C}^{\text{nv}} &= \begin{pmatrix} 0 \\ 0 \\ p \frac{\partial \alpha_g}{\partial x} + F_g^{\text{nv}} \\ p \frac{\partial \alpha_l}{\partial x} + F_l^{\text{nv}} \end{pmatrix} & \mathbf{S} &= \begin{pmatrix} 0 \\ 0 \\ \alpha_g \rho_g g_x + F_g^D \\ \alpha_l \rho_l g_x + F_l^D \end{pmatrix} \end{aligned} \quad (3)$$

where α_k is the volume fraction of phase k (called void fraction for the gas phase and often denoted simply by α), with $\alpha_g + \alpha_l = 1$, ρ_k and u_k are the density and velocity of phase k , and p is the pressure, common to both phases. F_k^{nv} represents the interfacial forces which contain differential terms, g_x represents the projection of the gravity vector onto the x -coordinate axis, and F_k^D the interfacial drag force.

The system (1)–(3) is closed by EOS for the liquid and gas phases. In this work, we will assume that the gas phase is governed by the isentropic perfect gas EOS, whereas the liquid phase is governed by the so-called Tait's EOS, which can be obtained from the stiffened gas EOS (used in the next section) assuming constant entropy. Thus, for the gas, we have:

$$p = p(\rho_g) = C \left(\frac{\rho_g}{\rho_g^o} \right)^\gamma \quad (4)$$

with the constants $\gamma = 1.4$, $C = 10^5$ Pa, $\rho_g^o = 1$ kg/m³ chosen as being representative of air. The speed of sound in the gas is given by the following expression:

$$a_g = \sqrt{\frac{\gamma p}{\rho_g}} \quad (5)$$

For the liquid, Tait's law reads:

$$p = p(\rho_l) = B \left[\left(\frac{\rho_l}{\rho_l^o} \right)^n - 1 \right] \quad (6)$$

with the following constants $n = 7.15$, $B = 3.3 \times 10^8$ Pa, $\rho_l^o = 1000$ kg/m³ chosen as being representative of water [29–31]. The speed of sound in the liquid is given by:

$$a_l = \sqrt{\frac{n}{\rho_l} (p + B)} \quad (7)$$

From a physical point of view, the vector of conservative variables \mathbf{U} is not a convenient state vector to work with. Indeed, initial and boundary conditions are more often than not specified in terms of primitive variables, such as pressure, temperature or void fraction. Furthermore, from a numerical point of view, and especially in the case of the AUSM+ scheme, primitive variables play a major role in the splitting and discretization of the fluxes. In the case of the four-equation isentropic model, we will therefore consider as primitive variables the vector \mathbf{V} defined as:

$$\mathbf{V} = (\alpha_g, u_g, u_l, p)^T \quad (8)$$

It is necessary to determine the transformation Φ between conservative and primitive variables, $\mathbf{V} = \Phi(\mathbf{U})$ and $\mathbf{U} = \Phi^{-1}(\mathbf{V})$. In general, this non-linear system of equations can be solved by a Newton–Raphson procedure. The velocities of each fluid can be readily deduced from the conservative variables. Denoting by U_i and V_i the i th components of the vectors \mathbf{U} and \mathbf{V} , one has:

$$u_g = \frac{U_3}{U_1}, \quad u_l = \frac{U_4}{U_2} \quad (9)$$

There remains to find α and p such that,

$$\alpha \rho_g(p) = U_1 \quad (10)$$

$$(1 - \alpha) \rho_l(p) = U_2 \quad (11)$$

Eliminating α from the second equation using the first equation, one obtains easily a non-linear equation $F(p) = 0$, with

$$F(p) = \left[1 - \frac{U_1}{\rho_g(p)} \right] \rho_l(p) - U_2 \quad (12)$$

which can be solved using a Newton–Raphson procedure. In practice, two or three iterations are required in each cell, at each time step, to converge the pressure to a few decimals.

2.3. Six-equation two-fluid model

The system of partial differential equations corresponding to the equal-pressure six-equation model is given by (1) with the vector of conserved variables, the flux and the source terms given by:

$$\begin{aligned} \mathbf{U} = & \begin{pmatrix} \alpha_g \rho_g \\ \alpha_l \rho_l \\ \alpha_g \rho_g u_g \\ \alpha_l \rho_l u_l \\ \alpha_g \rho_g E_g \\ \alpha_l \rho_l E_l \end{pmatrix} \quad \mathbf{F} = \begin{pmatrix} \alpha_g \rho_g u_g \\ \alpha_l \rho_l u_l \\ \alpha_g \rho_g u_g^2 + \alpha_g p \\ \alpha_l \rho_l u_l^2 + \alpha_l p \\ \alpha_g \rho_g u_g H_g \\ \alpha_l \rho_l u_l H_l \end{pmatrix} \\ \mathbf{C}^{nv} = & \begin{pmatrix} 0 \\ 0 \\ p \frac{\partial \alpha_g}{\partial x} + F_g^{nv} \\ p \frac{\partial \alpha_l}{\partial x} + F_l^{nv} \\ -p \frac{\partial \alpha_g}{\partial t} + u^{int} F_g^{nv} \\ -p \frac{\partial \alpha_l}{\partial t} + u^{int} F_l^{nv} \end{pmatrix} \quad \mathbf{S} = \begin{pmatrix} 0 \\ 0 \\ \alpha_g \rho_g g_x + F_g^D \\ \alpha_l \rho_l g_x + F_l^D \\ \alpha_g \rho_g u_g g_x + F_g^D u^{int} \\ \alpha_l \rho_l u_l g_x + F_l^D u^{int} \end{pmatrix} \end{aligned} \quad (13)$$

where, in addition to the variables defined in (3), E_k and H_k represent respectively the specific total energy and specific total enthalpy of phase k , with $H_k = E_k + p/\rho_k$, and u^{int} is an interfacial velocity which requires further modelling.

The system (1)–(13) is closed by the EOS for the gas and liquid phases. Here, we will assume that the gas phase is governed by the ideal gas law whereas the liquid phase is governed by a so-called stiffened gas law [32]. Thus we have

$$\begin{aligned} p(\rho_g, e_g) &= (\gamma_g - 1)\rho_g e_g \\ p(\rho_l, e_l) &= (\gamma_l - 1)\rho_l e_l - \gamma_l p_\infty \end{aligned}$$

with representative values of γ_g (air), γ_l and p_∞ (water) given by:

$$\gamma_g = 1.4, \quad \gamma_l = 2.8, \quad p_\infty = 8.5 \times 10^8 \text{ Pa}$$

For each fluid, the above EOS is a combination of a caloric EOS, $p = p(\rho, T)$ and thermal EOS, $e = e(\rho, T)$. For a perfect gas, it is well known that these equations take the form:

$$p(\rho_g, T_g) = \rho_g R_g T_g, \quad e_g(\rho_g, T_g) = \frac{R_g}{\gamma_g - 1} T_g \quad (14)$$

with $R_g = 288.2 \text{ J/kg/K}$ for air. The thermal and caloric EOS for a stiffened gas law are not as straightforward, and cannot be chosen independently. In particular, the EOS $p = p(V, T)$ and $e = e(V, T)$ where $V = 1/\rho$ is the specific volume, must satisfy the following compatibility relation:

$$\left(\frac{\partial e}{\partial V} \right)_T = -p + T \left(\frac{\partial p}{\partial T} \right)_V$$

We find in the case of the stiffened EOS the following expressions:

$$p(\rho_l, T_l) = \frac{\gamma_l - 1}{\gamma_l} \rho_l C_p T_l - p_\infty, \quad e_l(\rho_l, T_l) = \frac{C_p}{\gamma_l} T_l + \frac{p_\infty}{\rho_l} \quad (15)$$

where C_p is the specific heat capacity of liquid water, which we assume constant, $C_p \approx 4186 \text{ J/kg/K}$. The speed of sound in the gas phase is given by:

$$a_g(T_g) = \sqrt{\frac{\gamma_g p}{\rho_g}} = \sqrt{\gamma_g R_g T_g} \quad (16)$$

whereas in the liquid, one has:

$$a_l(T_l) = \sqrt{\gamma_l \frac{p + p_\infty}{\rho_l}} = \sqrt{(\gamma_l - 1) C_p T_l} \quad (17)$$

Fig. 1 shows the comparison between the analytical EOS for liquid (Tait's EOS for the isentropic model (3)) and the stiffened gas EOS for the six-equations model (13)) and National Institute of Standards and Technology (NIST, <http://www.nist.gov>) data for water, for various temperatures at 1 bar, and for various pressures at 323 K. The agreement is qualitatively correct and may be refined further by “tuning” the constants appearing in the EOS. However, it is also clear that though sufficient in the context of numerical developments, the use of analytical EOS does not

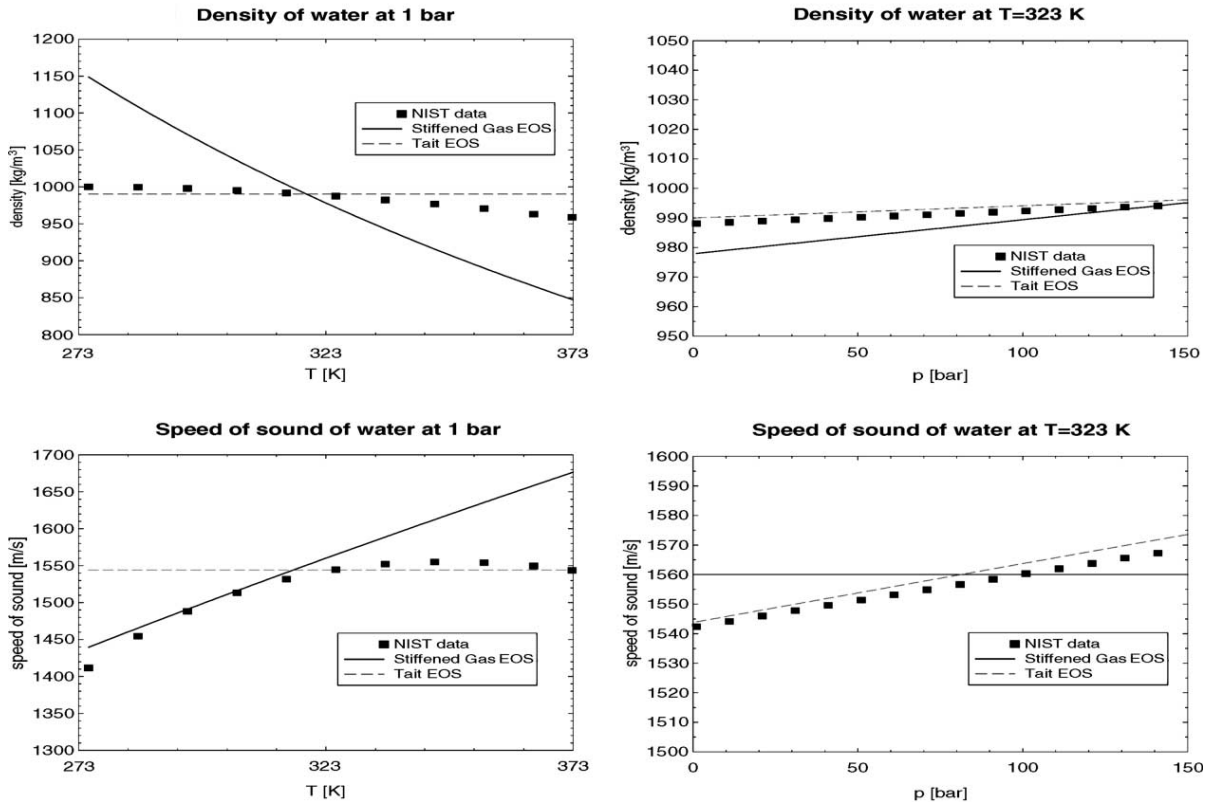


Fig. 1. Comparison between analytical EOS and NIST data. Density and speed of sound in liquid water as a function of temperature at 1 bar (left), and as a function of pressure at 323 K (right).

allow the modelling of phase change. For that, representative thermodynamic models for water must be used.

In terms of primitive variables, we shall consider the vector of physical variables,

$$\mathbf{V} = (\alpha_g, u_g, u_l, p, T_g, T_l)^T \quad (18)$$

As in the case of the isentropic two-fluid model, the transformation Φ between conservative and primitive variables, $\mathbf{V} = \Phi(\mathbf{U})$ and $\mathbf{U} = \Phi^{-1}(\mathbf{V})$, represents a non-linear system of equations which can be solved by a Newton–Raphson procedure. Here, the relatively simple form of the EOS allows the solution to be expressed in closed form, with pressure the (positive) root of a quadratic equation. One determines successively the velocities,

$$V_2 = u_g = \frac{U_3}{U_1}, \quad V_3 = u_l = \frac{U_4}{U_2} \quad (19)$$

the internal energies,

$$e_g = \frac{U_5}{U_1} - \frac{1}{2} \left(\frac{U_3}{U_1} \right)^2, \quad e_l = \frac{U_6}{U_2} - \frac{1}{2} \left(\frac{U_4}{U_2} \right)^2$$

the pressure,

$$\begin{aligned} A &= U_1(\gamma_g - 1)e_g, \quad B = U_2(\gamma_l - 1)e_l, \quad \Delta = (\gamma_l p_\infty - A - B)^2 + 4A\gamma_l p_\infty, \\ V_4 &= p = \frac{1}{2}[A + B - \gamma_l p_\infty + \sqrt{\Delta}] \end{aligned} \quad (20)$$

the void fraction,

$$V_1 = \alpha_g = \frac{A}{p} \quad (21)$$

and finally the temperatures,

$$V_5 = T_g = \frac{\gamma_g - 1}{R_g} e_g, \quad V_6 = T_l = \frac{\gamma_l e_l}{C_p \left(1 + \frac{p_\infty}{p + p_\infty} (\gamma_l - 1) \right)} \quad (22)$$

2.4. Interfacial transfer terms

The basic model ($F_k^{\text{nv}} \equiv 0$) being non-hyperbolic, interfacial force terms are often added to the system, in order to make it hyperbolic. There is quite a large literature on such regularising terms, their physical interpretation and their influence on the mathematical nature of the two-phase systems. We shall consider here an interfacial pressure correction force, of the form

$$F_k^{\text{nv}} = (p^{\text{int}} - p) \frac{\partial \alpha_k}{\partial x} \quad (23)$$

where p^{int} is the interfacial pressure given by [33]

$$p^{\text{int}} = p - \sigma \frac{\alpha_g \rho_g \alpha_l \rho_l}{\alpha_g \rho_l + \alpha_l \rho_g} (u_g - u_l)^2 \quad (24)$$

with σ a positive constant. Taking $\sigma \geq 1$ makes the two-fluid model hyperbolic.

The term $u^{\text{int}} F_k^{\text{nv}}$ requires the definition of the interfacial velocity u^{int} . In general, it is modelled as a weighted average of the gas and liquid velocity,

$$u^{\text{int}} = \beta u_g + (1 - \beta) u_l, \quad \beta \in [0, 1] \quad (25)$$

Possible choices of β are $\beta = \frac{1}{2}$ or $\beta = \alpha_g$. Quite often though, the term $u^{\text{int}} F_k^{\text{nv}}$ is neglected in the energy equation.

As far the interfacial drag term is concerned, its expression depends very much on the topology of the flow, and many different expressions can be found in the literature. Here, the following expression will be used:

$$F_g^D = -C_f \alpha_g (1 - \alpha_g) \rho_g (u_g - u_l), \quad F_l^D = -F_g^D \quad (26)$$

where C_f is a positive constant.

3. Space and time discretizations

The system (1) is discretized using a three-point stencil and forward Euler time-stepping, leading to a scheme of the form,

$$\mathbf{U}_j^{n+1} = \mathbf{U}_j^n - \frac{\Delta t}{\Delta x} [\mathbf{F}^\star(\mathbf{U}_j^n, \mathbf{U}_{j+1}^n) - \mathbf{F}^\star(\mathbf{U}_{j-1}^n, \mathbf{U}_j^n)] + \Delta t [(\mathbf{C}^{\text{nv}})_j^n + \mathbf{S}_j^n] \quad (27)$$

where $\mathbf{F}^\star(\mathbf{U}_L, \mathbf{U}_R)$ is the AUSM+ numerical flux function, defined at the interface separating two states, \mathbf{U}_L and \mathbf{U}_R , with the subscripts L and R denoting the left and the right of the interface. In the present paper only a first-order version of the scheme will be considered in which U_L and U_R are the states in the cells immediately adjacent to the interface.

Δt is the time-step, based on a volume-fraction weighted average of “acoustic”-type signals,

$$\Delta t = \text{CFL} \times \min_j \left[\frac{(1-\alpha)\Delta x}{|(u_l)_j| + (a_l)_j} + \frac{\alpha\Delta x}{|(u_g)_j| + (a_g)_j} \right] \quad (28)$$

where CFL is a CFL-like number. Depending on the test cases discussed in Section 4, values of CFL between 0.1 and 0.9 were used.

3.1. The AUSM+ scheme for the two-fluid model

As for its single phase counterpart described in [1,7,10], the two-fluid AUSM+ scheme which we propose is based on a decomposition of the flux appearing in (1) in a convective part, associated to the mass flux and a pressure term. Thus in the case of the six-equation model and for each phase k , denoting by \mathbf{F}_k the corresponding flux and $\dot{m}_k = \alpha_k \rho_k u_k$ the mass flux, one has:

$$\mathbf{F}_k = \begin{pmatrix} \alpha_k \rho_k u_k \\ \alpha_k \rho_k u_k^2 + \alpha_k p \\ \alpha_k \rho_k u_k H_k \end{pmatrix} = \dot{m}_k \begin{pmatrix} 1 \\ u_k \\ H_k \end{pmatrix} + \begin{pmatrix} 0 \\ \alpha_k p \\ 0 \end{pmatrix} = \dot{m}_k \Psi_k + \mathbf{P}_k \quad (29)$$

The numerical flux at the interface separating the left state \mathbf{U}_L and the right state \mathbf{U}_R simply reads:

$$\mathbf{F}_k^\star(\mathbf{U}_L, \mathbf{U}_R) = \dot{m}_k^\star \Psi_k^\star + \mathbf{P}_k^\star \quad (30)$$

where simple upwinding based on the sign of \dot{m}_k^\star is used to compute Ψ_k^\star ,

$$\dot{m}_k^\star \Psi_k^\star = \frac{1}{2} \dot{m}_k^\star [\Psi_k(\mathbf{U}_L) + \Psi_k(\mathbf{U}_R)] + \frac{1}{2} |\dot{m}_k^\star| [\Psi_k(\mathbf{U}_L) - \Psi_k(\mathbf{U}_R)] \quad (31)$$

The AUSM+ scheme for a two-fluid ($k = g, l$) flow therefore requires only the evaluation of two scalars for each phase, \dot{m}_k^\star and $(\alpha_k p)^\star$.

- In a first step, a numerical speed of sound at the interface is defined, and left and right Mach numbers based on that numerical speed of sound are computed. Different choices of numerical speeds of sound were investigated by Liou [10]. Here, we will consider:

$$a_k^\star = \sqrt{(a_k)_L (a_k)_R}, \quad (M_k)_L = \frac{(u_k)_L}{a_k^\star}, \quad (M_k)_R = \frac{(u_k)_R}{a_k^\star} \quad (32)$$

- In a second step, the pressure at the interface is computed as a weighted average of the left and right pressures,

$$(\alpha_k p)^* = \mathcal{P}^+((M_k)_L)(\alpha_k p)_L + \mathcal{P}^-((M_k)_R)(\alpha_k p)_R \quad (33)$$

where \mathcal{P}^\pm are polynomial functions, satisfying properties of consistency, differentiability and symmetry. One must note however that $(\alpha_k p)^*$ does not necessarily lie in the interval between $(\alpha_k p)_L$ and $(\alpha_k p)_R$, since $\mathcal{P}^+(x) + \mathcal{P}^-(y) \neq 1$ in general.

- In a third and last step, a numerical Mach number at the interface is computed as a polynomial function of the left and right Mach numbers,

$$M_k^* = \mathcal{M}^+((M_k)_L) + \mathcal{M}^-((M_k)_R) \quad (34)$$

where \mathcal{M}^\pm are polynomial functions. The mass flux is then defined as:

$$\dot{m}_k^* = a_k^* \left((\alpha_k \rho_k)_L \frac{M_k^* + |M_k^*|}{2} + (\alpha_k \rho_k)_R \frac{M_k^* - |M_k^*|}{2} \right) \quad (35)$$

The polynomials \mathcal{M}^\pm and \mathcal{P}^\pm used in this study are the same as those of the original AUSM+ scheme [1], namely:

$$\mathcal{M}_1^\pm = \frac{1}{2}(M \pm |M|) \quad (36)$$

$$\mathcal{M}_2^\pm = \begin{cases} \mathcal{M}_1^\pm & \text{if } |M| \geq 1 \\ \pm \frac{1}{4}(M \pm 1)^2 & \text{else.} \end{cases} \quad (37)$$

$$\mathcal{M}^\pm = \begin{cases} \mathcal{M}_1^\pm & \text{if } |M| \geq 1 \\ \mathcal{M}_2^\pm(1 \mp 16B\mathcal{M}_2^\mp) & \text{else.} \end{cases} \quad (38)$$

$$\mathcal{P}^\pm = \begin{cases} \mathcal{M}_1^\pm/M & \text{if } |M| \geq 1 \\ \pm \mathcal{M}_2^\pm(2 \mp M - 16AM\mathcal{M}_2^\mp) & \text{else.} \end{cases} \quad (39)$$

with $A = 3/16$ and $B = 1/8$.

3.2. Low Mach number flow

It is well-known that for single phase flow, density-based solvers experience stiffness problems as well as a loss of accuracy when approaching the low Mach number limit. This is especially apparent when computing thermal-hydraulic flows in boiling systems with compressible solvers such as described in [27]. Preconditioning strategies, first developed for the Euler equations of gas dynamics (see for instance [34,35]), were recently extended to Roe-type solvers for the two-phase HEM [12]. Similarly, modifications of the AUSM+ scheme were recently proposed in [10] to provide high accuracy at all speeds, for real fluid flows including two-phase homogeneous equilibrium flow.

The analysis of the spatial discretization of the modified AUSM+ scheme discussed in [6] or [36] emphasizes the necessity to couple the pressure and the velocity field at low speeds since in such a case AUSM+ behaves more as a central difference discretization, which raises the possibility of odd-even decoupling. This is especially important when computing flows of almost pure

water, which, though treated as a compressible medium, is characterised by speeds of sound of the order of 10^3 m/s, and in most applications, by Mach numbers of the order of 10^{-3} . The mass flux of the liquid phase is therefore modified by adding a pressure diffusion term \dot{m}_p to its baseline expression (35):

$$\widetilde{\dot{m}}_l^\star = \dot{m}_l^\star + \dot{m}_p \quad (40)$$

The pressure diffusion term is designed so as to ensure a sufficient level of dissipation when the Mach number of the liquid phase tends to zero. Following [36], we proceed as follows:

- redefine the interface numerical speed of sound (32) and corresponding left and right Mach numbers,

$$\widetilde{a}_l^\star = f^\star \left(\frac{1}{2} \left[\frac{(u_l)_L}{(a_l)_L} + \frac{(u_l)_R}{(a_l)_R} \right] \right) \sqrt{(a_l)_L (a_l)_R} \quad (41)$$

$$\widetilde{(M_l)_L} = \frac{(u_l)_L}{\widetilde{a}_l^\star}, \quad \widetilde{(M_l)_R} = \frac{(u_l)_R}{\widetilde{a}_l^\star} \quad (42)$$

with f^\star a “scaling” factor defined as,

$$f^\star(M) = \frac{\sqrt{(1 - M_o^2)^2 M^2 + 4 M_o^2}}{1 + M_o^2} \quad (43)$$

and M_o a “cut-off” Mach number, typically of the order of 10^{-4} .

- compute $\mathcal{M}^\star = \mathcal{M}^+((\widetilde{M_l})_L) - \mathcal{M}_1^+((\widetilde{M_l})_L) - \mathcal{M}^-((\widetilde{M_l})_R) + \mathcal{M}_1^-((\widetilde{M_l})_R)$
- evaluate the pressure diffusion term defined as

$$\dot{m}_p = \frac{1}{2} \widetilde{a}_l^\star \left(\frac{1}{M_o^2} - 1 \right) \mathcal{M}^\star \frac{(\alpha_l)_L p_L - (\alpha_l)_R p_R}{(a_l^\star)^2} \quad (44)$$

The above expression for \dot{m}_p ensures the amount of dissipation introduced by this pressure diffusion term scales properly when the Mach number of the liquid phase tends to zero. Note this added dissipation was only required for some of the following test-cases, namely the phase-separation and oscillating manometer problems, with fine computational grids, on which the standard dissipation of the AUSM+ method is not sufficient.

3.3. Model for phase appearance and disappearance

Phase appearance and disappearance can represent a major numerical difficulty for a multi-fluid method, just as the formation of vacuum can test the robustness of a single-phase numerical method. One important aspect of the problem lies in the evaluation of the dissipation of the scheme when the void fraction tends either to zero or to one. In the case of the AUSM+ scheme, it is easy to check that the numerical fluxes F_k^\star remain non-singular as $\alpha_k \rightarrow 0$ or 1, as long as the Mach numbers $(M_k)_{L,R}$ remain bounded. For that condition to be fulfilled, the velocity u_k , determined from the conservative variables (9) or (19), must remain bounded. From a physical

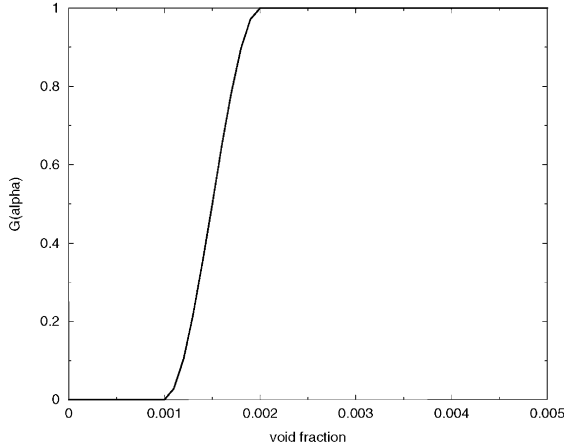


Fig. 2. Function $G(\alpha)$ used to enforce mechanical and thermal coupling of the vanishing phase with the remaining phase.

point of view, it can be argued that the velocity of the vanishing phase should tend towards the velocity of the remaining phase, which is well defined. For example, in the case where $\alpha \rightarrow 0$, one can compute the gas velocity as

$$u_g = G(\alpha) \frac{U_3}{U_1} + (1 - G(\alpha)) \frac{U_4}{U_2} \quad (45)$$

where $G(\alpha)$ is a positive function, equal to 1.0 for $\alpha > \alpha_{\min}$, with α_{\min} very close to zero, and tending to zero smoothly for $\alpha < \alpha_{\min}$. Such a function is represented in Fig. 2. In general, a value α_{\min} of the order of 10^{-4} was used in the computations. A similar treatment is applied to the temperature of the vanishing phase. Note that no cut-off is actually applied to the void fraction itself.

An alternative to this approach, which we have not investigated yet, is the method developed for the CATHARE two-phase flow code [37], which involves the use of particular forms of interfacial mass and energy transfer terms to guarantee that the void fraction remains in the interval $[\alpha_{\min}, \alpha_{\max}]$, together with interfacial friction terms to model the mechanical coupling of the residual phases.

3.4. Discretization of source terms

We treat the non-conservative terms as source terms, and in particular, independently of the convective terms. This is not the approach followed in the methods based on Approximate Riemann solvers [27], where upwinding of the non-conservative terms is advocated. We believe our simple strategy—central discretization of all source terms—is justified by the performance of the method on the test cases discussed in Section 4.

The interfacial source terms \mathbf{C}^{nv} are discretized in a very simple manner. Terms of the form $p(\partial\alpha_k/\partial x)$ are discretized centrally in space. Thus, at node j and time level n ,

$$\left(p \frac{\partial\alpha_k}{\partial x} \right)_j^n = p_j \frac{(\alpha_k)_{j+1}^n - (\alpha_k)_{j-1}^n}{2\Delta x}$$

Terms of the form $p(\partial\alpha_k/\partial t)$ are discretized at time level n as

$$\left(p \frac{\partial \alpha_k}{\partial t} \right)_j^n = p_j \frac{(\alpha_k)_j^n - (\alpha_k)_j^{n-1}}{\Delta t^{n-1}}$$

so as to keep the scheme explicit in time. This only requires storing the time-step from the previous iteration.

The gravity source terms in \mathbf{S} are also discretized very simply, in an explicit manner. Thus, at node i and time level n ,

$$\begin{aligned} (\alpha_k \rho_k g_x)_j^n &= (\alpha_k)_j^n (\rho_k)_j^n g_x \\ (\alpha_k \rho_k u_k g_x)_j^n &= (\alpha_k)_j^n (\rho_k)_j^n (u_k)_j^n g_x \end{aligned}$$

Finally, the interfacial drag terms, F_k^D , are also discretized centrally,

$$(F_k^D)_j^n = \pm C_f \alpha_j^n (1 - \alpha_j^n) (\rho_g)_j^n ((u_g)_j^n - (u_l)_j^n)$$

3.5. Boundary conditions

Boundary conditions are implemented very simply using the well-known “ghost cell” approach, whereby the inlet and outlet boundaries are represented by interfaces separating the first and last computational cells from fictitious cells whose states are defined by a combination of imposed and extrapolated values. For convenience, primitive variables are used rather than conservative variables.

In one dimension, three types of boundary conditions must be considered:

- inlet: in general, we impose all quantities except pressure, which is extrapolated from the first computational cell;
- outlet: in general, we impose only pressure, usually at atmospheric conditions, and extrapolate the void fraction, the velocities and the temperatures from the last computational cell;
- wall: in that case, the ghost cell is a “mirror” cell, with the same values of void fraction, pressure and temperatures as the interior cell, but with opposite velocities.

4. Numerical results

In this section, the AUSM+ scheme is applied to a series of standard test cases documented in the literature. Here we shall focus only on two-fluid test cases—results using the HEM can be found in [10,15].

4.1. Ransom’s water faucet problem

In this test case, described in [38] and depicted in Fig. 3, the motion of a water column under the effect of gravity is simulated. The physical phenomenon reproduced in this benchmark problem is the acceleration of the liquid column under the action of gravity, which causes a

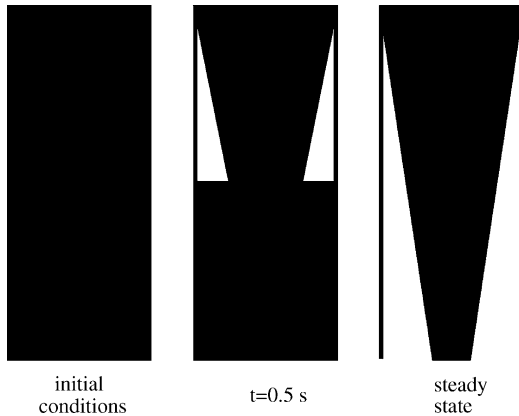


Fig. 3. Water faucet problem.

narrowing of the jet and the propagation of a void wave downwards and out of the domain (steady state). Thus, there is a decoupling of the motion of the liquid and the gas, which requires the use of a two-fluid model. Since energy transfers play no role, either the four-equation model or the six-equation model can be used, with or without an interfacial pressure correction term. The interfacial drag is set to zero ($C_f = 0$).

At time $t = 0$ s, the tube is uniformly filled with a two-phase mixture with void fraction $\alpha_o = 0.2$, liquid velocity $(u_l)_o = 10$ m/s, gas velocity $(u_g)_o = 0$ m/s, and pressure $p_o = 10^5$ Pa. As far as boundary conditions are concerned, the void fraction and the liquid and gas velocities are imposed at the inlet, equal to their initial values, and pressure is extrapolated from the computational domain. At the outlet, the pressure is imposed, equal to 10^5 Pa, while all other quantities are extrapolated from the interior domain.

This problem admits an analytical solution, derived under the assumptions that the liquid is incompressible and that variations of pressure in the liquid may be neglected. This yields the following expression for the void fraction profile $\alpha(x, t)$:

$$\alpha(x, t) = \begin{cases} 1 - \frac{(1 - \alpha_o)(u_l)_o}{\sqrt{(u_l)_o^2 + 2gx}} & \text{if } x < \frac{gt^2}{2} + (u_l)_o t \\ \sqrt{(u_l)_o^2 + 2gx} & \\ 0.2 & \text{else.} \end{cases} \quad (46)$$

4.1.1. Grid convergence study

Fig. 4 on the left shows a grid-convergence study of the void fraction profile, at time $t = 0.5$ s, computed with the AUSM+ scheme and the non-hyperbolic six-equation model, together with a comparison with the analytical profile. This plot shows typical first order behaviour in terms of spatial accuracy, and bears very close resemblance to Toumi's results using an Approximate Riemann solver and a hyperbolic model [20]. In the case of the AUSM+ scheme though, satisfactory results are obtained with the non-hyperbolic model on all but the finest mesh, where clear undershoots and overshoots are visible. We emphasize that these oscillations are not of numerical nature, but rather of mathematical nature, related to the ill-posedness of the non-hyperbolic

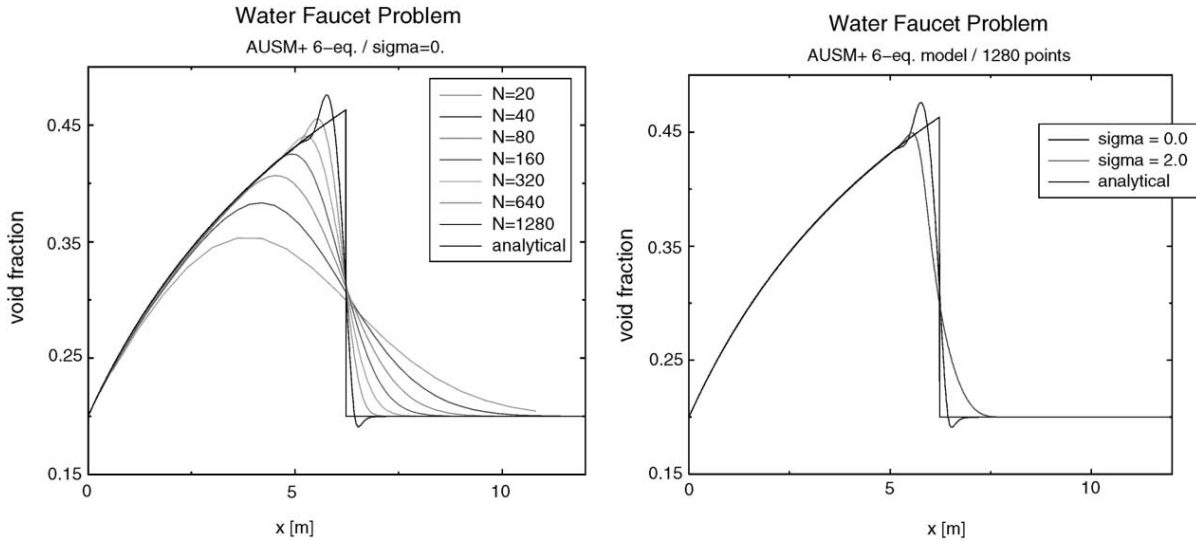


Fig. 4. Ransom's water faucet problem (time $t = 0.5$ s): grid convergence study with the non-hyperbolic ($\sigma = 0.0$) six-equation model (left); comparison between the non-hyperbolic model ($\sigma = 0.0$) and hyperbolic model ($\sigma = 2.0$), on the finest mesh (right).

two-fluid system. Fig. 4 on the right shows the regularising or dissipative effect of introducing a pressure correction term ($\sigma = 2.0$), i.e. using a hyperbolic model.

4.1.2. Time evolution study

Fig. 5 shows the time evolution of the void fraction profile (left) and the gas and liquid velocities (right) on a mesh of 320 points, computed with the non-hyperbolic six-equation model. In terms of void fraction profile and as for the grid-convergence study, close agreement with the solution of the Approximate Riemann solver [20] is observed. The acceleration of the liquid column (time evolution of u_l) is also clearly visible, from 10 m/s at the inlet to more than 18 m/s at the outlet, at “steady state”.

4.1.3. Comparison between four-equation and six-equation models

As was mentioned previously, this test case can be run with either the four-equation or the six-equation models. Fig. 6 shows the comparison between the two models on the 320-point grid, at time $t = 0.5$ s. Hardly any difference is observed on the void fraction profiles or on the liquid velocity profiles, and only a small difference is observed on the gas velocity profiles near the outlet.

4.2. Toumi's water-air shock tube problem

In this test case, a two-fluid shock tube problem is considered [20,39], in which the liquid phase is water governed by the stiffened gas EOS, and the gas phase is air governed by the perfect gas

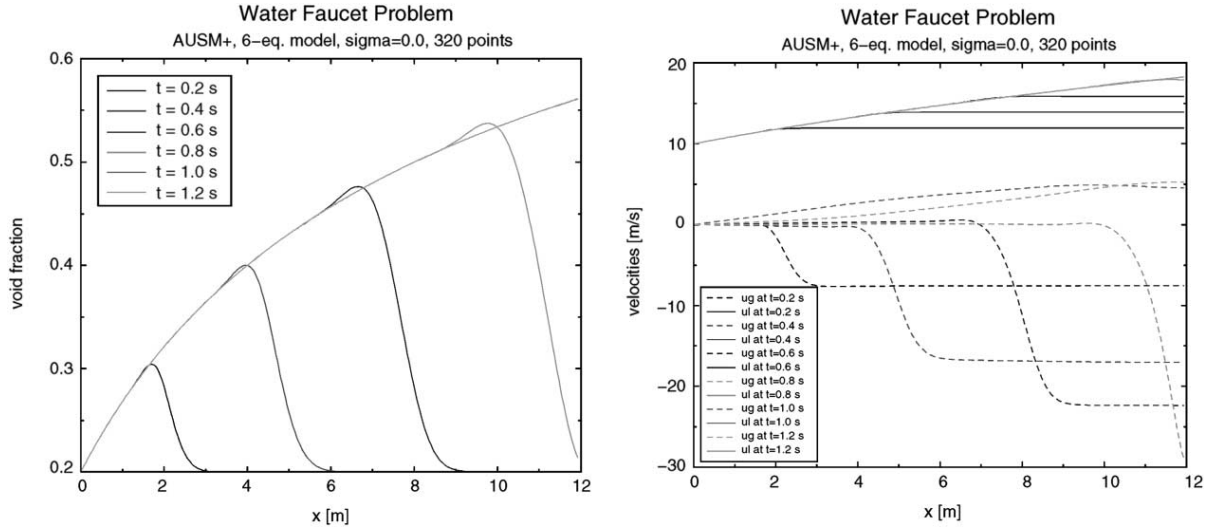


Fig. 5. Ransom's water faucet problem: time evolution of void fraction (left) and gas and liquid velocities (right), using the AUSM+ scheme, six-equation non-hyperbolic model ($\sigma = 0.0$), on a mesh of 320 points.

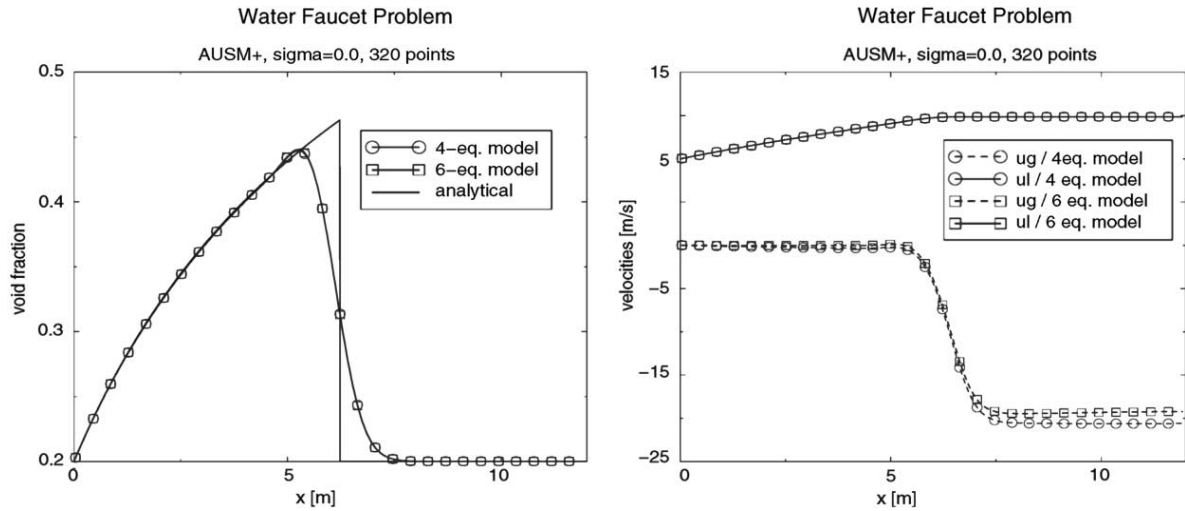


Fig. 6. Ransom's water faucet problem: comparison between four-equation and six-equation model. Void fraction (left) and gas and liquid velocities (right).

EOS. As was noted in [20], the time-dependent solution, which consists of six travelling waves separating seven constant states, depends on the eigenstructure of the system. Here, we will choose to model the hyperbolic two-fluid model with an interface pressure correction term of the form

(24) with $\sigma = 2.0$. Primitive states on either side of the diaphragm, located at $x = 5.0$, are defined as:

$$\mathbf{V}_L = \begin{pmatrix} 0.25 \\ 0 \\ 0 \\ 2 \times 10^7 \\ 308.15 \\ 308.15 \end{pmatrix}, \quad \mathbf{V}_R = \begin{pmatrix} 0.10 \\ 0 \\ 0 \\ 1 \times 10^7 \\ 308.15 \\ 308.15 \end{pmatrix}$$

All computations are performed up to time $t = 0.006$ s.

4.2.1. Grid convergence study for the AUSM+ scheme

Since no analytical solution is available, a grid convergence study is performed in order to gain some insight into the structure of the solution. A series of seven meshes, from 100 nodes to 10 000 nodes, has been considered in this study. From the results, plotted in Fig. 7, one can identify five constant states, an expansion-like wave propagating to the far left in the high pressure region, a shock-like wave propagating to the far right in the low pressure region, and contact-like waves in the middle of the structure, through which pressure remains approximately constant but the temperatures of the two fluids vary sensibly. This structure is perhaps best observed from the gas temperature profile computed on the finest mesh, plotted in Fig. 8.

4.2.2. Effect of interfacial pressure correction terms

As mentioned previously, the structure of the Riemann problem depends on the eigenstructure of the system, and therefore on the presence and form of all differential terms in the governing equations. The interfacial pressure correction term is one such term, characterised by the parameter σ . Three computations were performed on a mesh of 3200 nodes, using the AUSM+ method, and for three values of σ : 1.0, 2.0 and 5.0. The results are shown in Fig. 9, which shows the gas velocity and temperature profiles at $t = 0.006$ s.

Clearly, the speeds of the “shock” and “expansion” waves are almost unaffected by the value of σ , unlike the wave strengths. The internal structure of the solution on the other hand is sensibly modified, with variations in speeds and magnitude of the “contact” waves. Similar observations were made in [20], where solutions to this problem were computed with an Approximate Riemann solver.

4.3. Saurel's water-air shock tube problem

This test case is based on the water-air shock tube problem described in [25]. The length of the tube is 1 m, with the diaphragm, located at $x = 0.7$, separating almost pure water on the left from almost pure air on the right. The water is governed by the stiffened gas EOS, with parameters $\gamma_l = 4.4$ and $p_\infty = 6 \times 10^8$ Pa, whereas the air is governed by the perfect gas EOS. The pressure

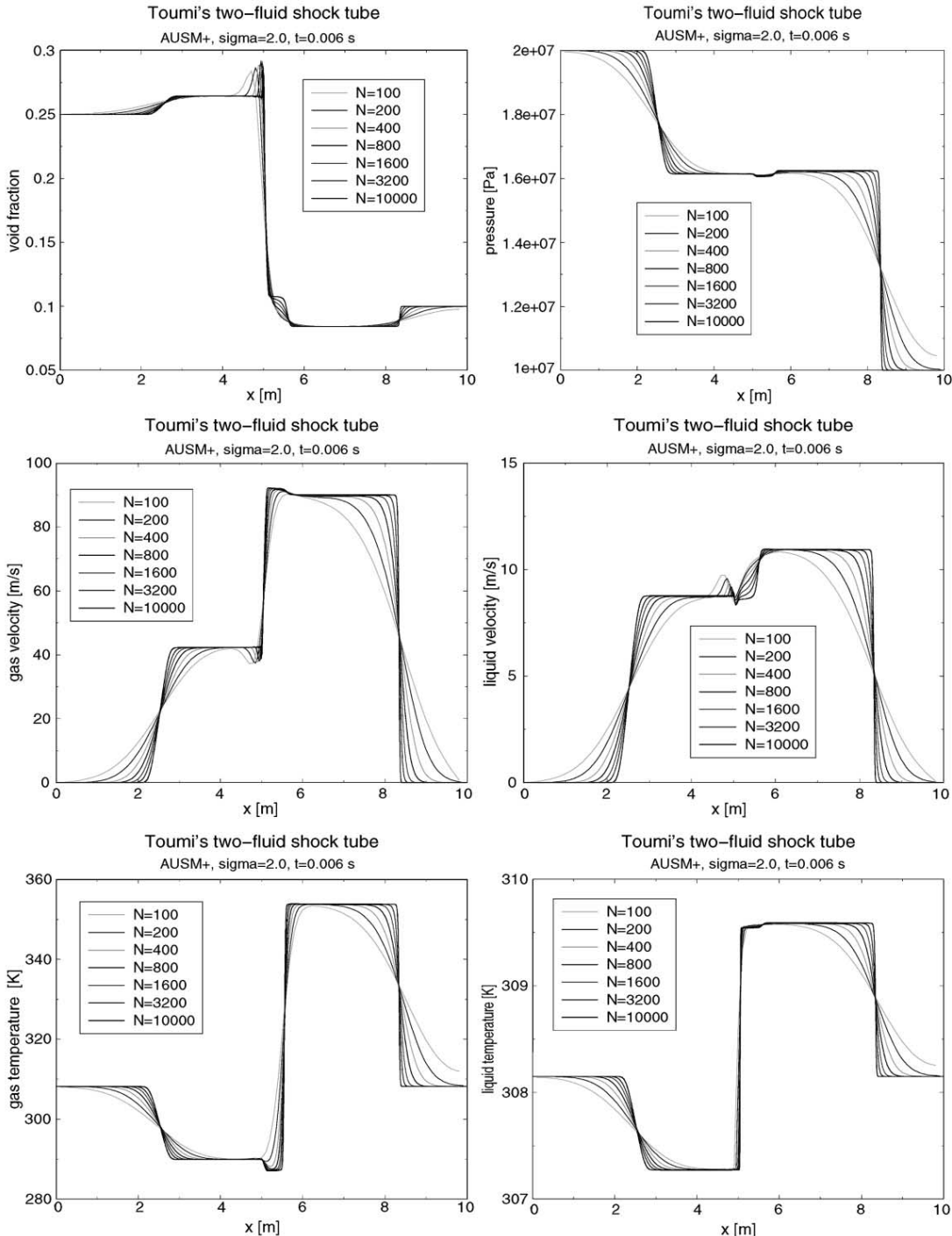


Fig. 7. Two-fluid shock tube problem: grid convergence study with the AUSM+ scheme, $\sigma = 2.0$. From top to bottom, left to right, void fraction, pressure, gas velocity, liquid velocity, gas temperature and liquid temperature.

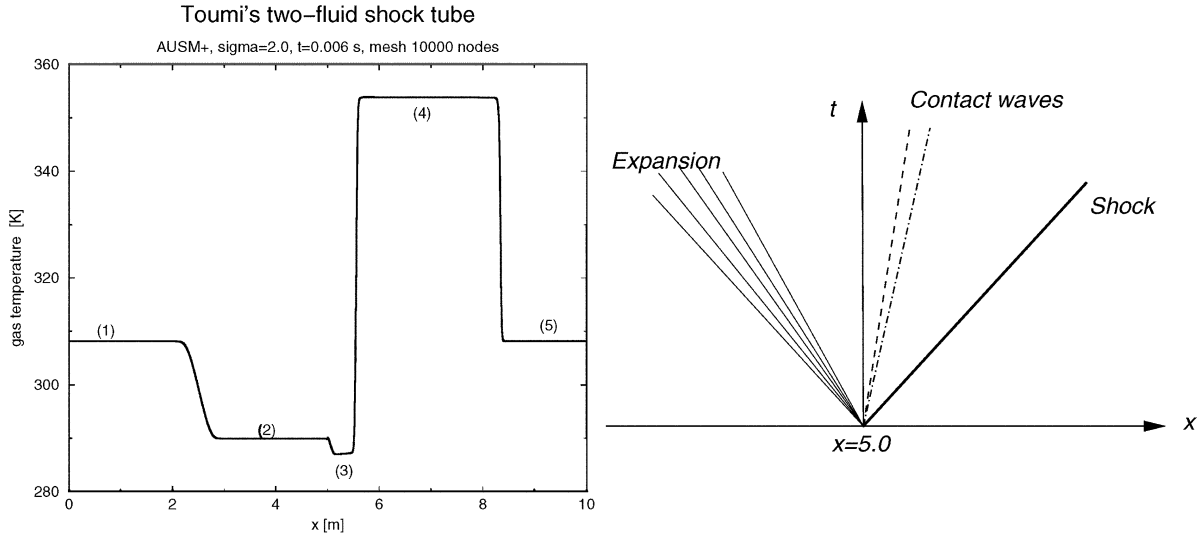


Fig. 8. Two-fluid shock tube problem: gas temperature profile on the finest mesh (10 000 nodes), showing the wave structure as computed with the AUSM+ scheme, $\sigma = 2.0$.

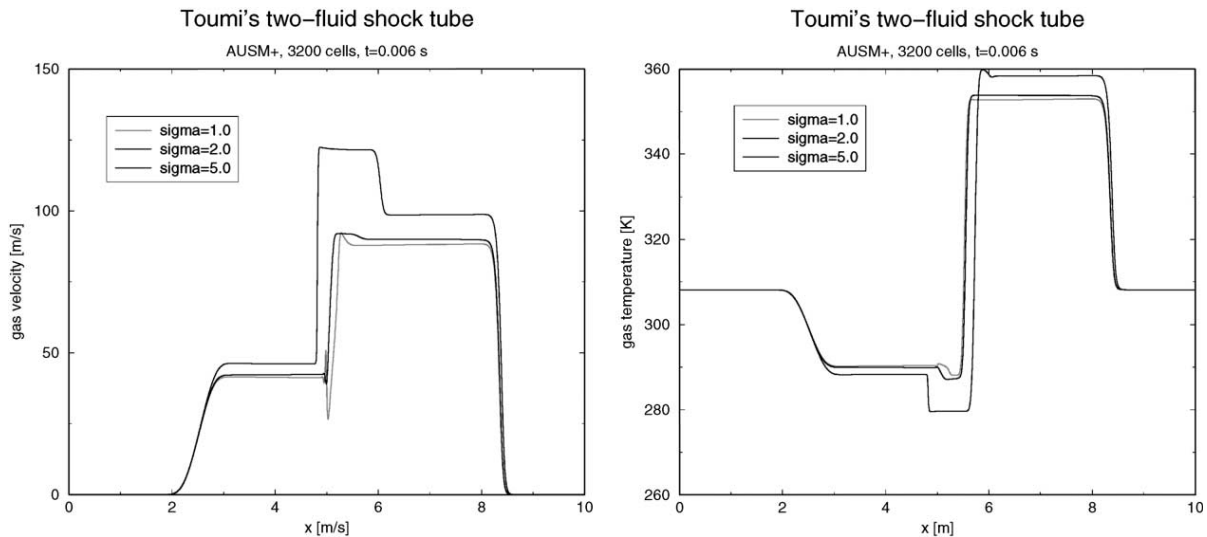


Fig. 9. Two-fluid shock tube problem. Effect of interfacial pressure correction terms on structure of the solution: gas velocity (left) and temperature (right) profiles, computed with the AUSM+ scheme.

ratio in this shock tube problem is 10^4 , making this test case particularly challenging. In terms of primitive variables, the conditions of the two fluids are defined as:

$$\mathbf{V}_L = \begin{pmatrix} \epsilon \\ 0 \\ 0 \\ 10^9 \\ 495 \\ 495 \end{pmatrix}, \quad \mathbf{V}_R = \begin{pmatrix} 1 - \epsilon \\ 0 \\ 0 \\ 10^5 \\ 7 \\ 7 \end{pmatrix}$$

These conditions correspond to a density of water of about 1000 kg/m^3 , and a density of air of about 50 kg/m^3 . In [25], computations are performed with a value $\epsilon = 10^{-8}$. In our case, we have been unable to run the schemes in a satisfactory way with such a small value of void fraction, and have therefore chosen the value $\epsilon = 10^{-3}$. Results, shown in Fig. 10, correspond to a computation performed with the AUSM+ scheme, on a grid of 100 mesh points, and with a hyperbolic two-fluid model ($\sigma = 2.0$). In a qualitative and quantitative way, these results compare well with those of Saurel and Abgrall [25] on the same mesh.

4.4. Phase separation test case

In this test case, also reported in [23], a homogeneous mixture consisting of water and air is separated under the action of gravity. The length of the tube is 7.5 m, with the coordinate system chosen such that $x = 0$ corresponds to the top of the vertical tube, and $x = 7.5$ corresponds to the bottom. “Wall” boundary conditions are applied at either end. The initial void fraction of the mixture is 0.5, pressure is set to 1 bar, and gas and liquid velocities are set to zero. The test case is depicted in Fig. 11.

A mesh of 100 points is considered. The computation is carried out until steady state is reached. From Fig. 12, which show the time evolution of the void fraction profiles, we observe that the interface separating the gas and liquid phases remains stationary for $t > 1.2$ s. At time $t = 2$ s, the residuals for both the vapour mass and liquid mass conservation equations have dropped more than four orders of magnitude, and we consider the solution at that time as the steady state solution. As shown in Fig. 13, the gas and liquid phases are well separated, with a void fraction below 2×10^{-4} in the region of “pure” liquid, and a void fraction above 0.995 in the region of pure air.

Fig. 14 (left) shows the pressure profile at steady state, showing that in the liquid, the theoretical hydrostatic pressure profile is well computed by the scheme.

4.5. Oscillating manometer

In this last test case, described in [38], the motion of a water column oscillating under the action of gravity is simulated. A U-shaped tube is considered, with both extremities open to the atmosphere, at 1 bar. The overall length of the tube is 20 m, and the length of the part occupied by the liquid is 10 m.

As initial conditions, depicted in Fig. 15, we assume that the levels of water in the two legs are at the same height, and that the velocities of both fluids are equal to $V_0 = 2.1 \text{ m/s}$. The pressure profile in the liquid is assumed to follow the hydrostatic pressure profile. The void fraction is taken equal to 0.001 inside the water column, and 0.999 outside. This gives:

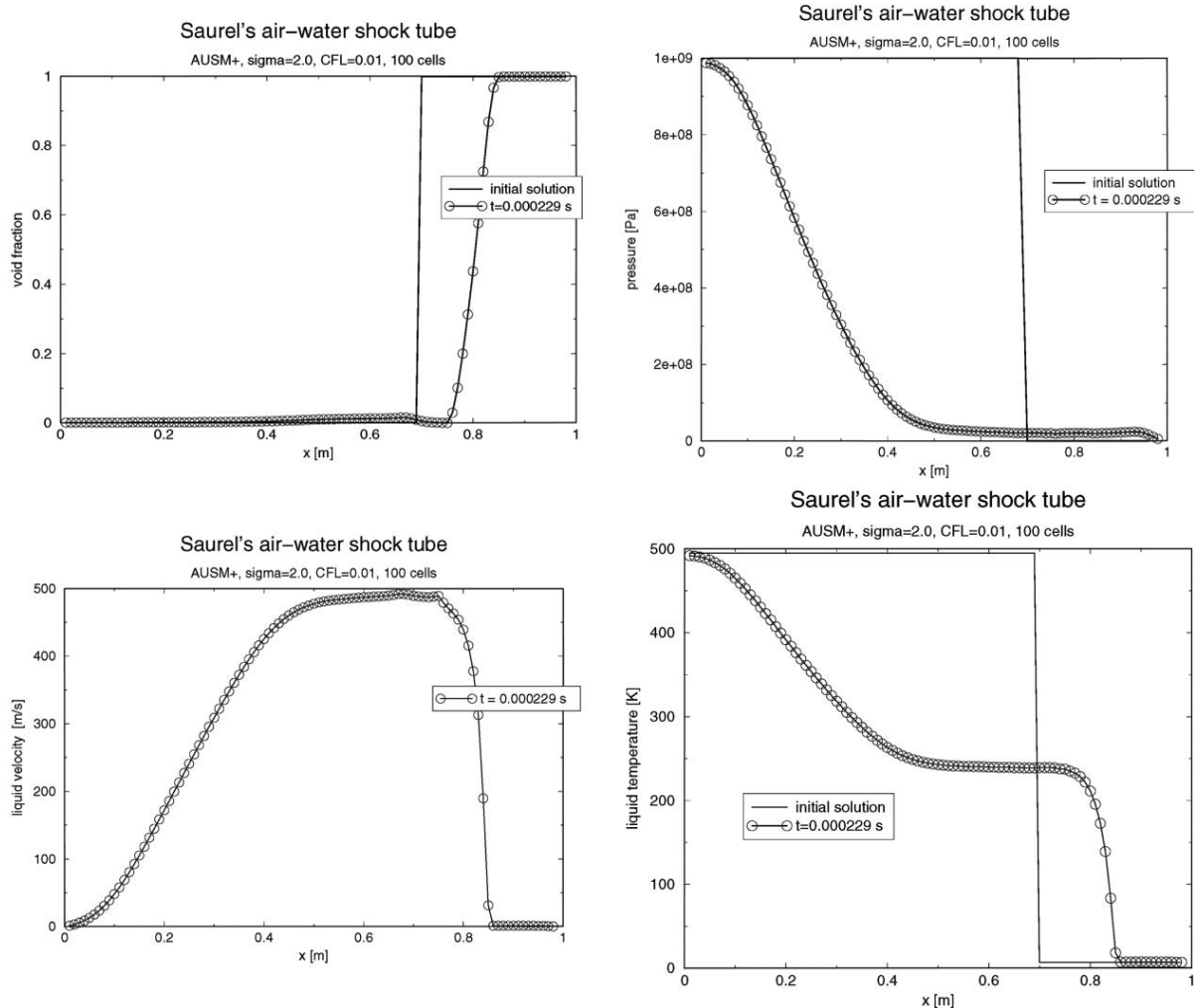


Fig. 10. Saurel's air–water shock tube. Results with AUSM+ scheme on a mesh of 100 cells. From top to bottom, left to right: void fraction, pressure, liquid velocity and liquid temperature.

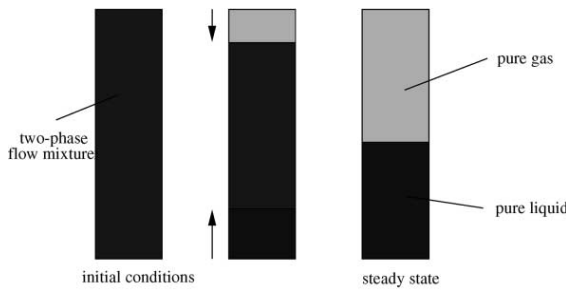


Fig. 11. Phase separation test case.

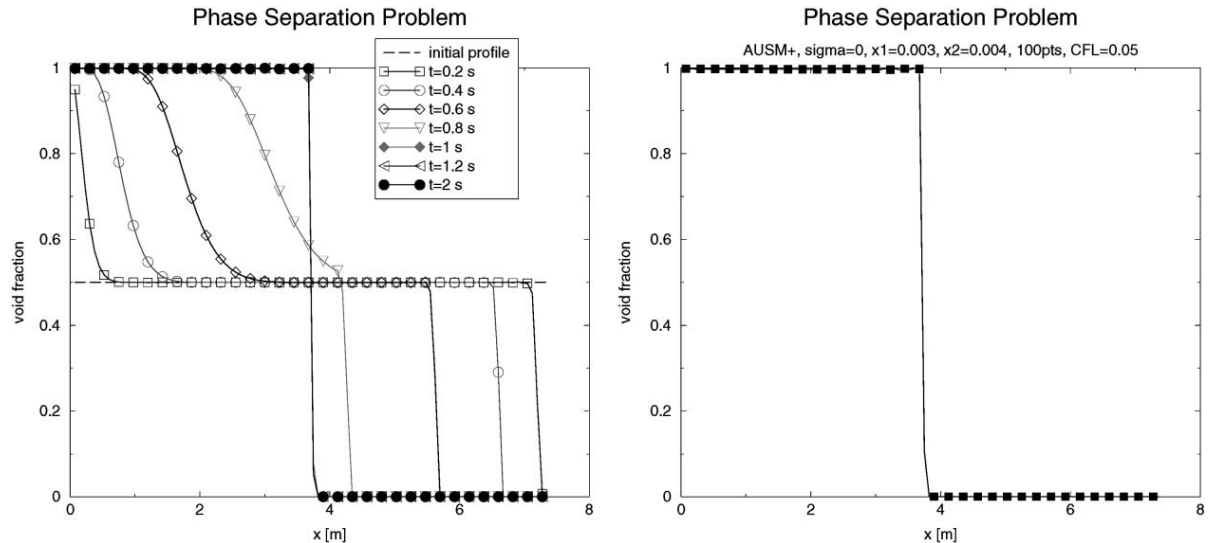


Fig. 12. Phase separation: evolution of the void fraction profiles as a function of time, and steady state profile.

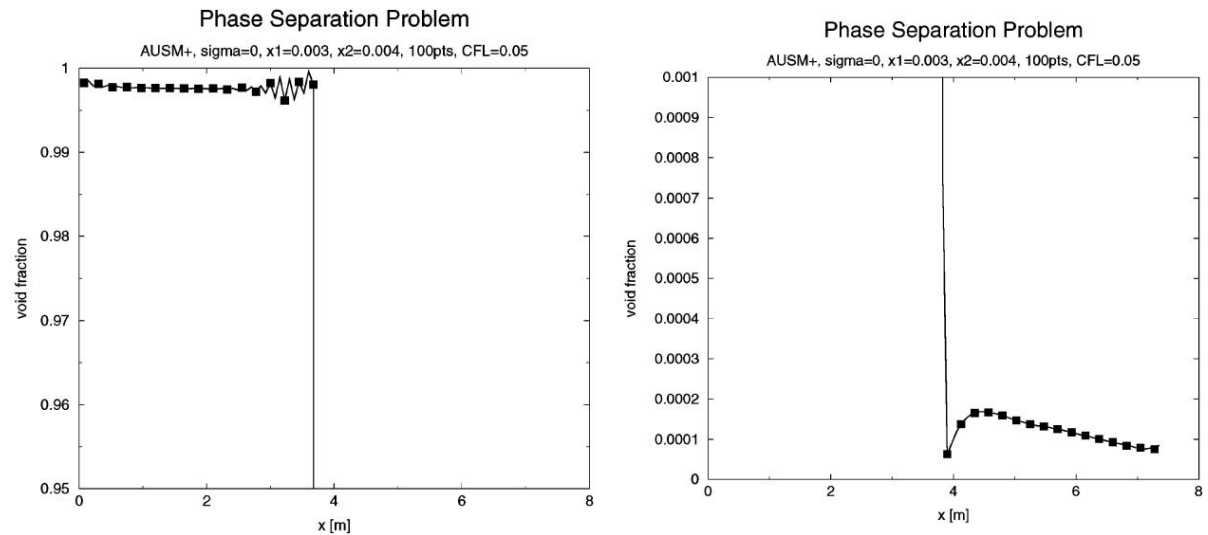


Fig. 13. Phase separation: detail of the void fraction profiles near the top wall (almost pure gas) and bottom wall (almost pure liquid).

$$\mathbf{V}(x, 0) = \begin{cases} (0.999, 2.1, 2.1, 10^5)^T & \text{if } 0 \leq x < 5 \\ \left(0.001, 2.1, 2.1, 10^5 + (\rho_l)_o g \frac{L}{\pi} \sin\left(\frac{\pi(x-5)}{L}\right)\right)^T & \text{if } 5 \leq x \leq 15 \\ (0.999, 2.1, 2.1, 10^5)^T & \text{if } 15 < x \leq 20 \end{cases}$$

with $(\rho_l)_o = 1000 \text{ kg/m}^3$ and $L = 10 \text{ m}$, and in terms of the gravity force,

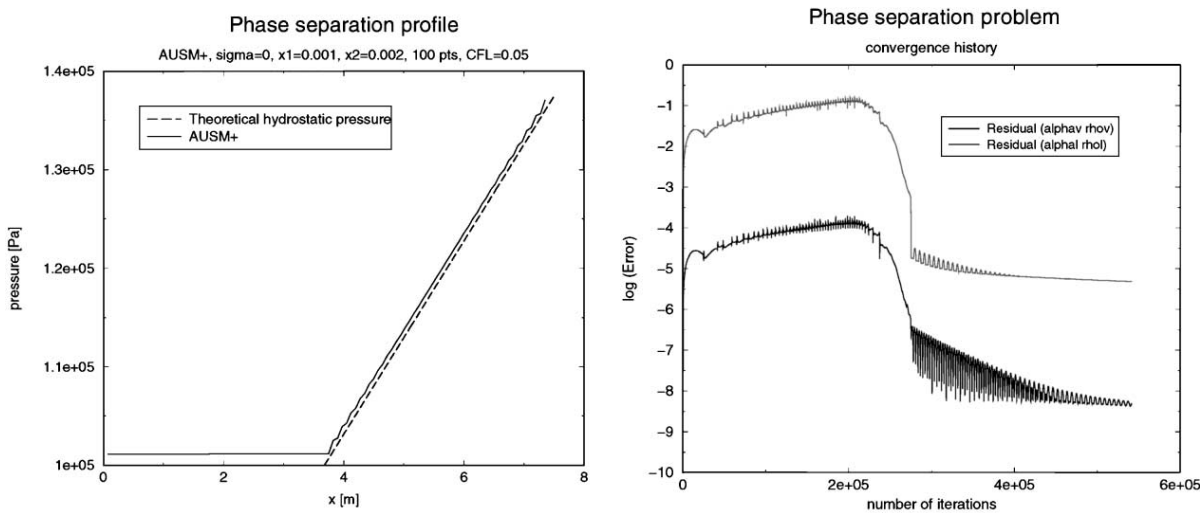


Fig. 14. Phase separation: pressure profile at steady state and convergence histories.

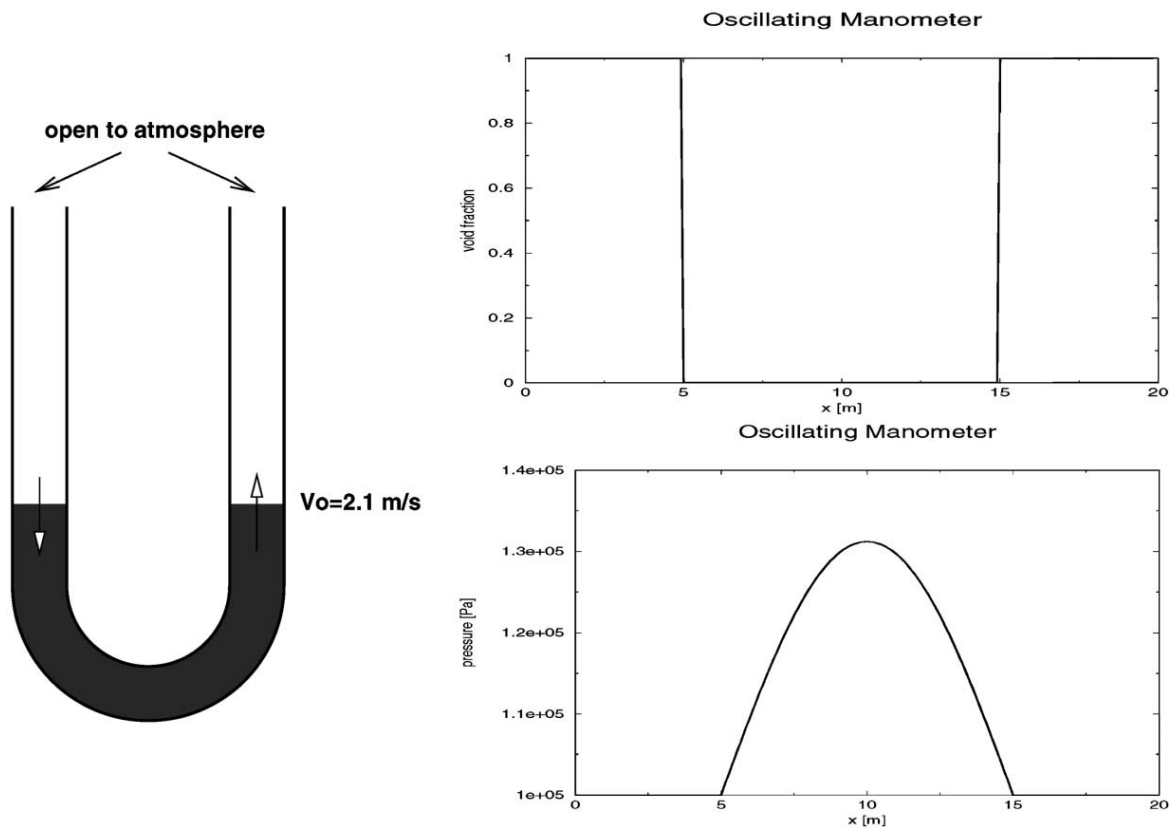


Fig. 15. Oscillating manometer: initial conditions.

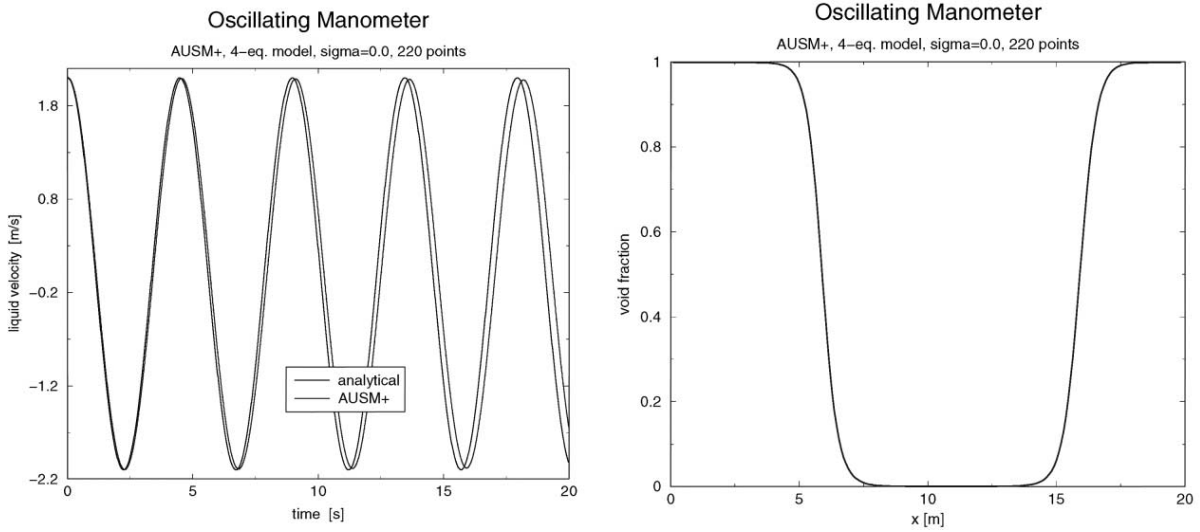


Fig. 16. Oscillating manometer: liquid velocity at the bottom of the tube as a function of time (left) and void fraction profile at time $t = 20$ s (right).

$$g_x(x) = \begin{cases} 9.81 & \text{if } 0 \leq x < 5 \\ 9.81 \cos \left[\frac{(x-5)}{10} \pi \right] & \text{if } 5 \leq x \leq 15 \\ -9.81 & \text{if } 15 < x \leq 20 \end{cases}$$

This problem admits an analytical solution, given by:

$$u_l(t) = V_0 \cos(\omega t), \quad \omega = \sqrt{\frac{2g}{L}} \quad (47)$$

The computation is performed up to time $t = 20$ s, with the non-hyperbolic four-equation model ($\sigma = 0.0$). A mesh of 220 points was used, together with a friction coefficient $C_f = 5 \times 10^4$ in the interfacial drag expression. Fig. 16 on the left shows the comparison between the computed liquid velocity (at $x = 10$ m corresponding to the bottom of the tube) and the analytical solution. Very little damping is observed, though the computed solution shows a slight phase error. The right figure shows the void fraction profile at time $t = 20$ s. A definite smearing of the initially sharp profile is clearly observed, an effect due to the interfacial drag.

5. Conclusions

In this paper, the AUSM+ scheme has been extended in a straight-forward manner to the basic single-pressure two-fluid model, using analytical equations of state to represent the gas and liquid phases. Non-conservative terms were treated as source terms, and discretized centrally in space. A number of two-fluid benchmark problems were successfully tested, showing the accuracy of the

method, and its ability to model flows over the whole range of void fraction and in particular stationary or moving interfaces.

Future work will include the incorporation of representative EOS for water and steam, so as to model mass and energy transfer due to phase change. Extension of the AUSM+ to multi-fluid models, consisting for example of one field to represent the gas phase, one field to represent the bulk liquid phase and a third field to represent a film of liquid with its own velocity field, can also be envisaged.

References

- [1] Liou MS. A sequel to AUSM: AUSM+. J Comput Phys 1996;129:364–82.
- [2] Darracq D, Champagneux S, Corjon A. Time-accurate fluid-structure coupling for turbulent flows. In: Bruneau C-H, editor. Sixteenth International Conference on Numerical Methods in Fluid Dynamics. Berlin: Springer; 1998. p. 31–6.
- [3] Luo H, Baum JD, Löhner R. A fast, matrix-free implicit method for compressible flows on unstructured grids. In: Bruneau C-H, editor. Sixteenth International Conference on Numerical Methods in Fluid Dynamics. Berlin: Springer; 1998. p. 73–8.
- [4] Radespiel R. Efficient computation of compressible flows. In: Bruneau C-H, editor. Sixteenth International Conference on Numerical Methods in Fluid Dynamics. Berlin: Springer; 1998. p. 237–53.
- [5] Liou M-S. Recent progress and applications of AUSM+. In: Bruneau C-H, editor. Sixteenth International Conference on Numerical Methods in Fluid Dynamics. Berlin: Springer; 1998. p. 302–7.
- [6] Edwards JR, Franklin RK, Liou MS. Low-diffusion flux-splitting methods for real fluid flows with phase transitions. AIAA Journal 2000;38(9):1624–33.
- [7] Liou MS. Mass flux schemes and connection to shock instability. J Comput Phys 2000;160:623–48.
- [8] Roe PL. Approximate Riemann solvers, parameter vectors & difference schemes. J Comput Phys 1981;43(2):357–71.
- [9] Osher S, Salomon F. Upwind schemes for hyperbolic systems of conservation laws. Math Comput 1982;38:339–74.
- [10] Liou MS, Edwards JR. AUSM schemes and extensions for low mach and multiphase flow. In: VKI LS 1999-03, Computational Fluid Dynamics. 1999.
- [11] Toumi I. A weak formulation of Roe's approximate Riemann solver. J Comput Phys 1992;102:360–73.
- [12] Clerc S. Numerical simulation of the homogeneous equilibrium model for two-phase flow. J Comput Phys 2000;161:354–75.
- [13] Huang LC. Pseudo-unsteady difference schemes for discontinuous solutions of steady-state one-dimensional fluid dynamics problem. J Comput Phys 1981;42:195–211.
- [14] De Vuyst f, Ghidaglia J-M, Le Coq G. A numerical simulation of flows with changes of state and strong gradients using the HEM. In: AMIF-ESF Workshop 'Computing Methods for Two-Phase Flow', Aussois, France, January 12–14; 2000.
- [15] Paillère H, Kumbaro A, Viozat C, Clerc S, Broquet A, Corre C. A comparison of Roe, VFFC and AUSM+ schemes for two-phase water/steam flows. In: Toro EF, editor. Godunov methods: theory and applications. Kluwer Academic/Plenum Publishers; 2000 [Edited Review].
- [16] Shyue K-M. A fluid-mixture type algorithm for compressible multicomponent flow with van der Waals equation of state. J Comput Phys 1999;156:43–88.
- [17] Shyue K-M. A fluid-mixture type algorithm for compressible multicomponent flow with Mie–Grüneisen equation of state. October 2000. Submitted for publication.
- [18] Stewart HB, Wendorff B. Two-phase flow: models and methods. J Comput Phys 1984;56:363–409.
- [19] Harlow FH, Amsden AA. Numerical calculation of multiphase fluid flow. J Comput Phys 1975;17:19–52.
- [20] Toumi I. An upwind numerical method for two-fluid two-phase flow models. Nucl Sci Eng 1996;123:147–68.
- [21] Sainsaulieu L. Finite volume approximation of two-phase fluid flows based on an approximate Roe-type Riemann solver. J Comput Phys 1995;121:1–28.

- [22] Romate JE. An approximate Riemann solver for a two-phase flow model with numerically given slip relation. *Comput Fluids* 1998;27(4):445–77.
- [23] Coquel F, El Amine K, Godlewski E, Perthame B, Rascle P. A numerical method using upwind schemes for the resolution of two-phase flows. *J Comput Phys* 1997;136:272–88.
- [24] Cocchi JP, Saurel R. A Riemann problem based method for compressible multifluid flows. *J Comput Phys* 1997;137:265–98.
- [25] Saurel R, Abgrall R. A multiphase Godunov method for compressible multifluid and multiphase flows. *J Comput Phys* 1999;150:425–67.
- [26] Städtker H, Franchello G, Worth B. Numerical simulation of multi-dimensional two-phase flow based on flux vector splitting. *Nucl Eng Design* 1997;177:199–213.
- [27] Toumi I, Kumbaro A, Paillère H. Approximate Riemann solvers and flux vector splitting schemes for two-phase flow. In: VKI LS 1999-03, Computational Fluid Dynamics; 1999.
- [28] Pokharna H, Mori M, Ransom VH. Regularization of two-phase flow models: a comparison of numerical and differential approaches. *J Comput Phys* 1997;134:282–95.
- [29] Fedkiw RP, Aslam T, Merriman B, Osher S. A non-oscillatory Eulerian approach to interfaces in multimaterial flows (the ghost fluid method). *J Comput Phys* 1999;152:457–92.
- [30] Ivings MJ, Causon DM, Toro EF. On Riemann solvers for compressible liquids. *Int J Numer Meth Fluids* 1998;28:395–418.
- [31] Tang HS, Huang D. A second-order accurate capturing scheme for 1D inviscid flows of gas and water with vacuum zones. *J Comput Phys* 1996;128:301–18.
- [32] Harlow F, Amsden A. Fluid dynamics. Technical report, Los Alamos National Laboratory, 1971. LA-4700.
- [33] Bestion D. The physical closure laws in the CATHARE code. *Nucl Eng Design* 1990;124:229–45.
- [34] Turkel E. Preconditioned methods for solving the incompressible and low speed compressible equations. *J Comput Phys* 1987;72:277–98.
- [35] Turkel E, Fiterman A, van Leer B. Preconditioning and the limit of the compressible to the incompressible flow equations for finite difference schemes. In: Hafez M, Caughey D, editors. Computing the future: advances and prospects for computational aerodynamics. Wiley; 1994. p. 215–34.
- [36] Edwards JR. Low-diffusion flux splitting methods for flows at all speeds. *AIAA J* 1998;36(9):1610–7.
- [37] Bestion D. The phase appearance and disappearance in the CATHARE code. In: Proceedings of the Workshop on “Trends in Numerical and Physical Modelling for Industrial Multiphase Flows”, Cargèse, France, 27–29 September 2000.
- [38] Ransom VH. In: Multiphase science and technology, vol. 6; 1992.
- [39] Tiselić I, Petelin S. Modelling of two-phase flow with second-order accurate scheme. *J Comput Phys* 1997;136:503–21.